

Kinetic Simulations of Relativistic Radiative Magnetic Reconnection

José Ortuño-Macías¹ and Krzysztof Nalewajko¹

1. Nicolaus Copernicus Astronomical Center, Polish Academy of Sciences, Bartycka 18, 00-716 Warsaw, Poland

High energy astrophysical phenomena, such as blazars, gamma-ray bursts and pulsar wind nebulae, are associated with efficient particle acceleration sites because they show emission signatures of non-thermal particle distribution. Their common characteristic is strong magnetic field, which provides the condition for relativistic magnetic reconnection (RMR) to be the most efficient particle acceleration mechanism. By means of kinetic simulations it has been observed that during the reconnection process, highly energetic particles are enclosed within magnetic islands also termed as plasmoids. The properties of plasmoids have been studied through kinetic simulations with open boundaries where a steady-state RMR process was achieved. When the RMR outflows are unimpeded, a continuous chain of plasmoids is generated with stochastic plasmoid properties. A wide range of parameters has been used in order to model the emission properties of blazars, which are characterized by high variability and broad band spectrum. However, previous studies of plasmoid properties were based on simulations where emission effects have not been included. Recent work has shown that in the regime of high radiation efficiency the cooling affects the particle dynamics and thus it might also influence the generation of plasmoid chains. We performed 2D Particle-In-Cell (PIC) simulations of steady-state RMR with open boundaries with synchrotron radiation reaction and calculation of the resulting emission signatures from our computational domain. We find that the cores of the large-sized plasmoids are the main emission sites because of an increasing magnetic energy density and particle number density. The resulting synchrotron lightcurves reveal sharp flares originating from tail-on mergers between small/fast plasmoids and their large/slow targets.

1 Introduction

High energy astrophysical phenomena share in common strong and broad band synchrotron emission which comes from emission sites that are strongly magnetized. Furthermore the power spectral densities of such regions indicate that the emission is originated by non-thermal energy particle distribution. This high energy properties are even more conspicuous when the object is undergoing a flaring stage. One example are the flares from the Crab pulsar wind nebula observed on April of 2011 (Buehler et al., 2012), whose emission peaked over 375 MeV when the maximum energy limit for synchrotron emission is $\epsilon_{\max}^{\text{syn}} \simeq 160$ MeV (obtained from equation that acceleration and emission rates from regions where electric and magnetic fields are of the same order). Similarly for blazar flares we observe very high energy gamma rays with energies > 100 GeV at very short timescales of up to ~ 200 s (Albert et al. 2007, Aharonian et al., 2007) which indicates that emission sites are compact and host within the relativistic jet (Begelman et al., 2008).

Then highly efficient particle acceleration mechanism is required to reach such high energies. RMR has been probed by kinetic simulations to be able to strongly accelerate particles within high magnetic energy density regions over other mechanism as shocks (Sironi & Spitkovsky, 2014). The maximum energy peak of the Crab pulsar wind nebula flares was explained by such simulations showing that at the acceleration region of RMR the magnetic field is weaker than the accelerating electric field, and hence provides particle acceleration without being constrained by synchrotron emission losses (Cerutti et al., 2013).

Simulations show that particles, after being accelerated, are enclosed inside magnetic island called plasmoids. Simulations with open boundaries allow the outflow, originated due to the reconnection of magnetic field lines, to be unimpeded. Under such condition steady-state RMR is maintained providing a chain of plasmoids with stochastic distribution of properties (Sironi et al., 2016). Later work has made use of the resulting plasmoids properties variability obtained from simulations in order to model its radiative signatures and compare with blazars flares observational characteristics (Petropoulou et al. 2018, Christie et al. 2019, Christie et al. 2020).

However, recent PIC simulations which include cooling by emission effects have proved that in a high radiative efficiency configuration the capability for particle acceleration is decreasing (Nalewajko 2018, Schoeffler et al. 2019, Hakobyan et al. 2019). With the aim of studying plasmoid properties when affected by radiative cooling, we performed kinetic simulations of steady-state radiative RMR showing that the general picture established by Sironi et al. (2016) is confirmed, but the particle distribution inside plasmoids cannot be assumed as homogeneous where cores of large-sized plasmoids are the main emission sites and sharp flares are collected in the synchrotron lightcurves when tail-on mergers between small/fast plasmoid and a large/slow target plasmoid take place (Ortuño-Macías & Nalewajko, 2019).

2 Simulation setup

We make use of a custom version of the PIC code *Zeltron* (Cerutti et al., 2013) to perform 2D kinetic simulations of steady-state RMR in pair electron and positron plasma. The initial stage involves a single Harris-type current layer placed in the middle of the computational domain (Kirk & Skjæraasen, 2003):

$$\begin{aligned} B_{\text{ini},x} &= -B_0 \tanh(y/\delta), \\ n_d &= n_{d,0} \cosh^{-2}(y/\delta), \end{aligned} \tag{1}$$

where $B_{\text{ini},x}$ is the initial magnetic field component in the x-direction, B_0 is the characteristic value of the magnetic field strength, δ is the Harris layer half-thickness, n_d is the number density drifting particles that form the current layer and $n_{d,0}$ is the number density at the middle of the current layer corresponding to the equilibrium initial state.

In order to trigger the RMR process at the middle of the current layer, a small current and pressure gap is set driving that region to dynamical collapse. The steady state is achieved by open boundaries, where the particles are able to escape, the fields are absorbed, and particles are injected at rate that matches the initial density and current profiles. At every time step we perform the following operation:

$$\begin{aligned}\mathbf{B}(x) &\rightarrow \mathbf{B}(x) + \lambda(x)[\mathbf{B}_{\text{ini}}(x) - \mathbf{B}(x)], \\ \mathbf{E}(x) &\rightarrow \mathbf{E}(x) + \lambda(x)[\mathbf{E}_{\text{ini}}(x) - \mathbf{E}(x)],\end{aligned}\tag{2}$$

where $\lambda(x) = 0.5(|x - x_{\text{abs}}|/\Delta_{\text{abs}})^3$, x_{abs} is the position of the absorbing layer inner edge and Δ_{abs} is the field-absorbing layers thickness.

The synchrotron radiation signatures are computed at every time step, accounting for the radiation reaction force that emitting particles experience. Simultaneously, the spectral synchrotron emission from the particle ensemble is collected as it would be measured by two observers placed at the edges of the current layer where the relativistic outflowing plasma emission is beamed.

We explore high cooling efficiency by means of different plasma configurations of the particle temperature $\Theta = kT/mc^2$, where the nominal cooling length is of the order or smaller than the computational domain size, $l_{\text{cool}} < L_x$. Synchrotron cooling length is defined similar to Nalewajko (2018) with the initial background magnetic energy density $U_{B,0} = \langle B^2 \rangle / (8\pi) = B_0^2 / (8\pi)$,

$$l_{\text{cool}} = c\tau_{\text{cool}} = \frac{\langle \gamma \rangle}{\langle |d\gamma/cdt| \rangle} \simeq \frac{\langle \gamma \rangle}{\langle \gamma^2 \rangle} \frac{3m_e c^2}{4\sigma_T U_{B,0}} \simeq \frac{(3\pi/2)e}{\sigma_T \Theta^2 B_0} \rho_0,\tag{3}$$

where l_{cool} is the synchrotron cooling length, τ_{cool} is the synchrotron cooling time, γ is the Lorentz factor of the particles, σ_T is the Thomson cross section, Θ is the particle distribution temperature and ρ_0 is the plasma nominal gyroradius.

The results presented here correspond to simulations with plasma initial temperature set to different temperatures in order to explore different radiation efficiency regimes: $\Theta = 2 \times 10^5$, 5×10^5 , and 1.25×10^6 . The magnetization parameter defined as $\sigma_0 = B_0^2 / 4\pi mn_0 c^2$ is set to $\sigma_0 = 10$ and $\sigma_0 = 50$; and magnetic field $B_0 = 1$ G. The size of the computational domain in physical units is $L_x / \rho_0 = 1536$ where ρ_0 is the plasma nominal gyroradius given by $\rho_0 = \Theta m_e c^2 / (eB_0)$. The corresponding cooling length to domain size ratio is $l_{\text{cool}} / L_x \simeq 0.3$.

3 Results

The relevant information from the computational domain comes from the reconnecting layer placed at the middle of the domain. In order to store it every timestep, we averaged the properties in the y-direction of the reconnecting layer for a strip that contains it extending over $0 < x < L_x$ and $|y| < \delta/2$. The resulting x -profiles are superposed for every timestep and shown as spacetime diagrams as in the central panel of Fig. 3. Using the x -profiles of magnetic fields, magnetic potential and number density, we identified the plasmoids and differentiate two regions: their external layer and their internal core, where properties are substantially different as shown in Fig. 1.

Fig. 2 presents the histories of individual plasmoids compared for the four large simulations performed. We found that the densities of plasmoid cores grow systematically in time for all simulations. The larger the plasmoid is the denser its core becomes, reaching higher densities by the plasmoids from the simulation with higher temperature $\Theta = 1.25 \times 10^6$, i.e. with higher radiative efficiency. In the case of $\sigma_0 = 50$, the core densities scale roughly in proportion to σ_0 . The histories of

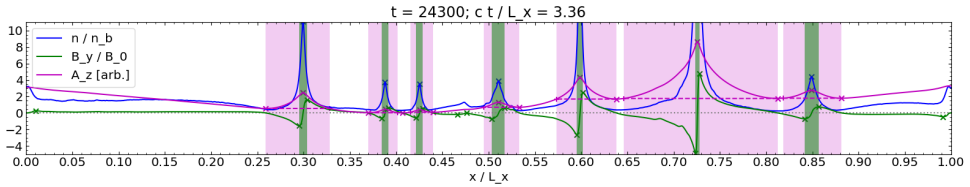


Fig. 1: Example of x -profiles of particle density (blue), magnetic field component B_y (green), and magnetic vector potential component A_z . The green vertical stripes mark the horizontal edges of plasmoid cores, and the light magenta areas mark the plasmoid layers.

plasmoid core velocities confirm the previous picture shown by Sironi et al. (2016) where large plasmoids are accelerated slowly only to mildly relativistic velocities and small ones rapidly get accelerated up to relativistic velocities. The mean particle energies of plasmoid cores measured in the zero-momentum frame (see Werner et al., 2018) are higher for large plasmoids until the radiative cooling effects become significant. On the other hand, the small-sized plasmoids keep a roughly constant value indicating not strong emission losses. Most of the plasmoids show an increasing synchrotron emissivity with time, which for large and medium plasmoids converges to their maximum values and for small plasmoids it decreases either slowly or rapidly at the end of their life.

In Fig. 3 we present the lightcurves observed at the edges of the current layer for the simulation with $\sigma_0 = 10$ and $\Theta = 5 \times 10^5$. Additionally, we show the spacetime diagram for the synchrotron emissivity power plotted in the middle with the same time y -coordinate as the lightcurves panels. It is shown at the figure, that the emission sites are the plasmoids where the small ones emit homogeneously and the large plasmoids have a clear different behaviour between the core and the external layer. The layers of large plasmoids show synchrotron power emission of similar order than the small-sized plasmoids.

The lightcurves show wide emission signatures corresponding to the large plasmoid cores approaching towards the edges. Due to the enhancement by relativistic beaming effect, the signals from the plasmoids traveling towards the observer will be the main source of emission. We can see that the bigger plasmoids produce larger amplitude and wider synchrotron signatures. It is also noticeable the presence of several rapid synchrotron flares with large amplitudes. Tracing back the black dashed lines of the spacetime diagram, which indicate the light path, we can identify these synchrotron flares with mergers between a small and fast plasmoid and a large and slow plasmoid.

4 Conclusions

We find similar general relation between the plasmoids acceleration and their size, i.e. large-sized plasmoids slowly accelerate up to mildly relativistic speeds while small-sized plasmoids get rapidly accelerated as established in Sironi et al. (2016). In previous models of blazar emission the properties of plasmoids were assumed to be homogeneous. For high synchrotron radiation efficiency, we show that there are two discernible regions inside the plasmoids, the core and the external layer. The

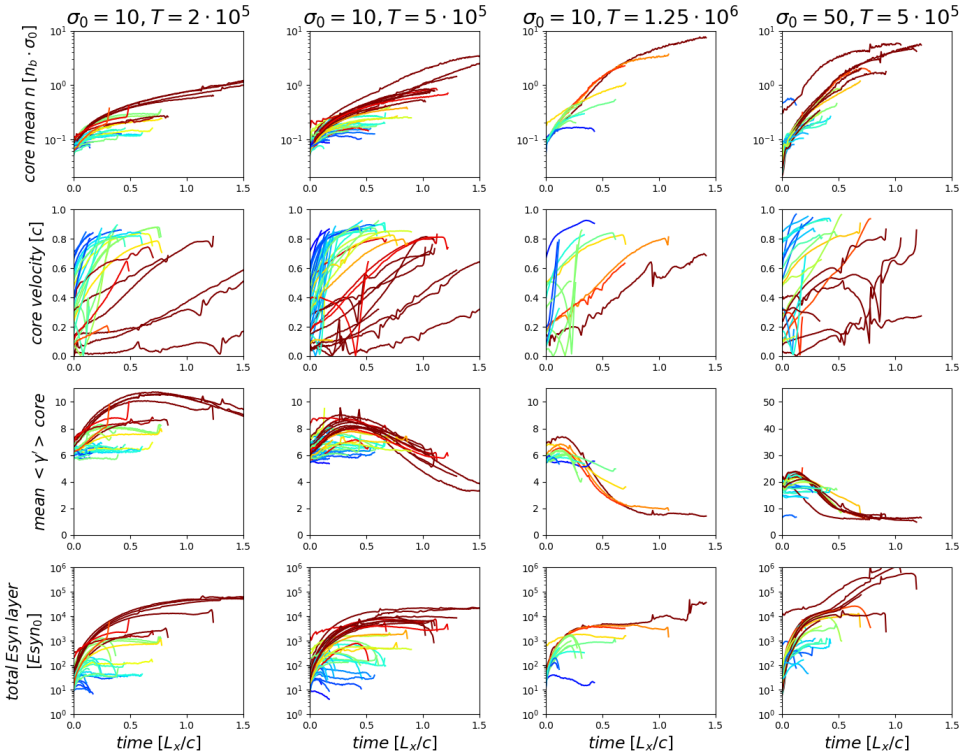


Fig. 2: Histories of individual plasmoids compared for the four large simulations. From top, the rows represent: (1) core mean density; (2) core velocity; (3) mean particle energy of the core in the zero-momentum frame; (4) total synchrotron emissivity. Line colors present the maximum size of the plasmoid reached during its life, dark red for large-sized plasmoids and dark blue for the smallest plasmoids.

main contribution to the emission is originated in the large plasmoid cores where due to radiative losses the density is enhanced. Despite the relativistic beaming, small plasmoids don't contribute significantly to synchrotron lightcurves. We find that total synchrotron radiation of the energy content of plasmoids cannot be contained in an open-boundaries simulation because the larger the computational domain is the more time the plasmoids can spend along the reconnecting layer and hence collect more energetic particles. Additionally to the signatures from large plasmoids outflowing towards the edges of the current layer, we observe that rapid synchrotron flares are produced when small/fast plasmoids collide with large/slow plasmoids.

Acknowledgements. These results are based on numerical simulations performed at the supercomputer *Prometheus* located at Cyfronet AGH, Poland (PLGrid grant recjose2018; PI: K. Nalewajko). This work was supported by the Polish National Science Centre grant 2015/18/E/ST9/00580.

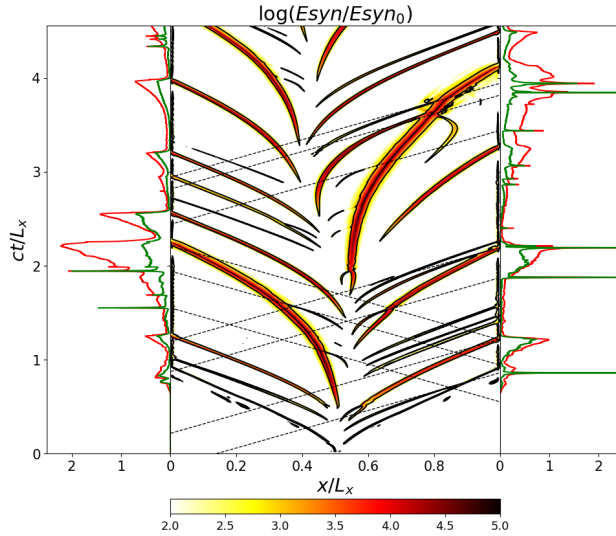


Fig. 3: Lightcurves and spacetime diagram of the simulation with $\sigma_0 = 10$ and $\Theta = 5 \times 10^5$. Left and right panels show synchrotron lightcurves measured by observers placed at left and right sides of the reconnecting layer, respectively. Red and green lines represent two different frequency bands, lower and higher frequency, respectively. The middle panel present the spacetime diagram of the total synchrotron power. Particle number density contours are shown in black indicating the edges of plasmoids. The black dashed lines represent the light-cones corresponding to selected features in either lightcurve.

References

- Aharonian, F., et al., *ApJ* **664**, 2, L71 (2007)
- Albert, J., et al., *ApJ* **669**, 2, 862 (2007)
- Begelman, M. C., Fabian, A. C., Rees, M. J., *MNRAS* **384**, 1, L19 (2008)
- Buehler, R., et al., *ApJ* **749**, 1, 26 (2012)
- Cerutti, B., Werner, G. R., Uzdensky, D. A., Begelman, M. C., *ApJ* **770**, 2, 147 (2013)
- Christie, I. M., Petropoulou, M., Sironi, L., Giannios, D., *MNRAS* **482**, 1, 65 (2019)
- Christie, I. M., Petropoulou, M., Sironi, L., Giannios, D., *MNRAS* **492**, 1, 549 (2020)
- Hakobyan, H., Philippov, A., Spitkovsky, A., *ApJ* **877**, 1, 53 (2019)
- Kirk, J. G., Skjæraasen, O., *ApJ* **591**, 1, 366 (2003)
- Nalewajko, K., *MNRAS* **481**, 4, 4342 (2018)
- Ortuño-Macías, J., Nalewajko, K., *arXiv e-prints* arXiv:1911.06830 (2019)
- Petropoulou, M., Christie, I. M., Sironi, L., Giannios, D., *MNRAS* **475**, 3, 3797 (2018)
- Schoeffler, K. M., et al., *ApJ* **870**, 1, 49 (2019)
- Sironi, L., Giannios, D., Petropoulou, M., *MNRAS* **462**, 1, 48 (2016)
- Sironi, L., Spitkovsky, A., *ApJ* **783**, 1, L21 (2014)
- Werner, G. R., et al., *MNRAS* **473**, 4, 4840 (2018)